Journal of Materials Chemistry A

Unveiling a High Capacity Multi-redox (Nb5+/Nb4+/Nb3+) NASICON-Nb2(PO4)3 Anode for Li- and Na-ion Batteries

Journal:	*Journal of Materials Chemistry A*
Manuscript ID	TA-ART-07-2022-005971.R1
Article Type:	Paper
Date Submitted by the Author:	17-Jan-2023
Complete List of Authors:	Patra, Biplab; JNCASR, New Chemistry Unit Kumar, Keshav; JNCASR, New Chemistry Unit Deb, Debolina; IISc, Department of Materials Engineering, Ghosh, Subham; JNCASR, New Chemistry Unit Sai Gautam, Gopalakrishnan; IISc, Materials Engineering Senguttuvan, Premkumar; JNCASR, New Chemistry Unit

SCHOLARONE™
Manuscripts

Unveiling a High Capacity Multi-redox ($Nb^{5+}/Nb^{4+}/Nb^{3+}$) NASICON-$Nb_2(PO_4)_3$ Anode for Li- and Na-ion Batteries

*Biplab Patra,[1] Keshav Kumar,[1] Debolina Deb,[2] Subham Ghosh,[1] Gopalakrishnan Sai Gautam,[2] and Premkumar Senguttuvan[1]**

[1]New Chemistry Unit, International Centre for Materials Science and School of Advanced Materials, Jawaharlal Nehru Centre for Advanced Scientific Research, Jakkur, Bengaluru-560064, India.

[2]Department of Materials Engineering, Indian Institute of Science, Bengaluru-560012, India.

Abstract: Sodium superionic conductors (NASICON)-type materials are widely explored as Li- and Na-ion cathodes and solid-state electrolytes but are largely ignored as anodes due to their lower capacities and higher intercalation voltages, which reduce the overall energy densities of Li- and Na-ion batteries (LIBs and SIBs). Herein, we unveil a high capacity multi-redox empty NASICON-$Nb_2(PO_4)_3$ as a potential anode material for LIBs and SIBs, which reversibly delivers 167 and 150 mAh g^{-1} at the average voltages of 1.86 V vs. Li^+/Li^0 and 1.46 V vs. Na^+/Na^0, respectively. The Li and Na intercalation reactions proceed *via* multiple phase transitions, leading to short-range ordered $Li_3Nb_2(PO_4)_3$ and triclinic ($P\bar{1}$) $Na_3Nb_2(PO_4)_3$, as revealed by *in-situ* X-ray diffraction studies. Our density functional theory calculations are also in agreement with the *in-situ* measurements in predicting a stable $Na_3Nb_2(PO_4)_3$ composition in the Na-$Nb_2(PO_4)_3$ pseudo-binary system. X-ray absorption spectroscopy confirms the participation of multi-redox $Nb^{5+}/Nb^{4+}/Nb^{3+}$ couples. The $Nb_2(PO_4)_3$ anode delivers capacities greater than 124 and 106 mAh g^{-1} at 1 C rate in Li and Na cells, respectively. Pairing $Nb_2(PO_4)_3$ with suitable cathodes and electrolytes can lead to high energy density batteries.

Introduction

The demand for low-cost and sustainable battery technologies is continuously increasing to achieve carbon neutrality.[1,2] At present, Li-ion batteries are used extensively in portable electronics, electric vehicles, and its Na-ion analogue has emerged as the front-runner for grid storage applications.[3–5] Nevertheless, there exist many technical challenges for improving the performance of such batteries, in terms of higher energy and power densities, enhanced safety, and long-term cyclability.[6,7] Since these performance metrics are deeply connected with the materials used, the need for advanced Li- and Na-ion electrodes and electrolytes is continuously growing.[8]

While graphite and hard carbon are widely used in commercial Li-ion and prototypical Na-ion cells, respectively, they pose a serious risk of lithium and sodium metal plating at higher current densities, besides their lower volumetric energy densities.[9] Alternatively, intercalation-type transition metal oxides insert lithium and sodium ions at relatively higher voltages (> 1.0 V), which may avoid electrolyte decomposition, and Li and Na metal electrodeposition.[10] In the case of LIBs,

$Li_4Ti_5O_{12}$ anode reversibly exchanges Li ions at 1.5 V vs. Li^+/Li^0 with a capacity of ~175 mAh g^{-1}.[11] Recently, Wadsley–Roth crystallographic shear phases such as $TiNb_2O_7$,[12,13] VNb_9O_{25}, [14] and $Ti_2Nb_{10}O_{29}$ [15] have gained much interest as Li-ion anodes due to their higher capacities (200-380 mAh g^{-1}) and excellent rate performances ($TiNb_2O_7$ delivers capacities of 236, 219, 195 and 128 mAh g^{-1} at 5, 10, 20 and 50 C rates, respectively). Similarly, few transition metal oxides such as $Na_2Ti_3O_7$,[16] TiO_2,[17] $Li_4Ti_5O_{12}$[18] have been investigated as potential Na-ion hosts with moderate capacities (100-170 mAh g^{-1}) and limited cycle life.

Apart from oxides, transition metal-based polyanionic compounds such as sodium superionic conductor (NASICON) frameworks have been explored as possible Li- and Na-ion anodes. NASICON frameworks are appealing as electrodes[19–23] and solid-electrolytes[24,25] for Li- and Na-ion battery applications owing to their higher chemical, structural and thermal stabilities, and higher Na-ion conductivity. Their general chemical composition can be given as $A_aM_2(XO_4)_3$ (A=Li and Na; M = Sc to Fe, Zr to Mo, In and Sn; X = Si, P, S; $0 \leq a \leq 4$) and structures are built by lantern units consisting of two MO_6 octahedra and three XO_4 tetrahedra, stacked along the *c*-axis.[26,27] Due to their size differences, Li and Na ions occupy different crystallographic sites in the NASICON framework (Li ions into 18f site of the $R\bar{3}$ & Na ions into 6b/18e sites of the $R\bar{3}c$).[28,29] In principle, NASICON compounds can reversibly exchange a maximum of four moles of Li and Na ions, if provided with suitable redox centers.

Experimentally, $ATi_2(PO_4)_3$ (A=Li and Na) NASICONs reversibly (de)intercalate two moles of Li- and Na-ions at 2.6 and 2.1 V vs. Li^+/Li^0 and Na^+/Na^0, respectively, through the redox activity of Ti^{4+}/Ti^{3+} couple.[30–32] Upon reducing the lower cut-off voltage beyond $Na_3Ti_2(PO_4)_3$, an additional mole of sodium can be intercalated at 0.45 V with concomitant reduction of Ti^{3+}/Ti^{2+}, accounting for a total capacity of 150 mAh g^{-1}.[33] Another NASICON-$Na_3V_2(PO_4)_3$ reversibly exchanges Na ions at a lower voltage (~1.6 V vs. Na) but shows the limited capacity of 60 mAh g^{-1} (i.e., equivalent of intercalation of one mole of sodium ions).[34,35] Also, a mixed NASICON compound, $TiNb(PO_4)_3$, has been preliminarily explored for Na intercalation (~120 mAh g^{-1}).[36] Thus, NASICON cathodes and anodes explored so far operate within the limit of three moles of lithium- and/or sodium-ion exchange during cycling, thus rendering maximum storage capacities of 140-160 mAh g^{-1}.[37–39] Moreover, in terms of synthesis, NASICONs usually contain Na (or Li)

ions as synthesized (e.g., $Na_3V_2(PO_4)_3$ is a NASICON composition that can be synthesized)[40] and electrochemical/chemical oxidation routes have to be employed to remove the Na (or Li)[41].

In this work, we report for the first time the synthesis of polycrystalline "empty" NASICON-$Nb_2(PO_4)_3$ and its potential application as an anode in LIBs and SIBs. Previously Leclaire *et al.* reported its crystal structure using a single crystal of $Nb_2(PO_4)_3$[42]. This compound contains no Li or Na ions in its pristine state and is expected to exchange higher amount (~3 moles per formula unit) of lithium and sodium ions through the activity of multi-redox-$Nb^{5+}/Nb^{4+}/Nb^{3+}$ centers at relatively lower voltages than the Ti- or V-based NASICON anodes. In addition to our electrochemical and characterization measurements, we have also performed first-principles calculations to understand the Na-intercalation phase behavior better. We believe that pairing this "empty" NASICON anode with suitable Na-ion cathodes and/or solid electrolytes (which can also be NASICON-based) can enable building high energy density Na-ion batteries.

Experimental

Synthesis:

Empty NASICON-$Nb_2(PO_4)_3$ were prepared by high-temperature solid-state synthesis. Nb_2O_5 (0.9 mmol) (Sigma Aldrich, 99.5%), P_2O_5 (1.5 mmol) (Alfa Aesar, 99.0%), Nb-powder (0.2 mmol) (Alfa Aesar, 99.8%) were mixed using a high-energy ball miller (SPEX 8000M) for 20 min. The resulting mixture was then placed in an evacuated quartz ampoule and sealed under high vacuum of 10^{-6} mbar. The tube was slowly heated up to 1473 K in 35 hours followed by dwelling at this temperature for 72 hours and then cooled back to room temperature in 7 hours. Finally, the tube was opened in an Ar-filled glove box and the final powder product was collected.

Characterization:

Synchrotron powder diffraction patterns were collected on $Nb_2(PO_4)_3$ and $Na_3Nb_2(PO_4)_3$ sealed in a Kapton capillary (0.5 mm diameter) at the 11-BM beamline (λ = 0.458969 Å) of Advanced Photon Source, Argonne National Laboratory, and the data were analyzed by FullProf program[43]. The FESEM images were taken using Zeiss (Gemini SEM 500) to observe the morphology and homogeneous distribution of the elements.

Electrochemical testing of $Nb_2(PO_4)_3$ was carried out in two-electrode Swagelok cells using either lithium or sodium (99.9% Aldrich) metal as the counter electrode in galvanostatic mode. The $Nb_2(PO_4)_3$ electrodes were prepared by ball milling as-synthesized samples with Super C45 (Timcal) in a 70:30 ratio for 8 min. The ball-milled mixture was collected and mixed with polyvinylidene fluoride (PVDF) (in such a way that the final electrode contains active material: carbon: PVDF in the weight ratio of 65:27:8) in N-methyl-2-pyrrolidone (NMP) solvent. The resulting slurry was uniformly coated on a Cu foil, followed by drying in a vacuum oven at 90 ℃ for 6 hours. The dried electrodes were punched into round discs of 10 mm dia. The active material loading of the final electrode was estimated as 2.5- 3.0 mg/cm^2. Sodium cells were assembled using a 1 M solution of $NaPF_6$ (Sigma, 98%) in diglyme Sigma, 99.5%) as an electrolyte with sodium metal as a counter electrode. Similarly, lithium cells were fabricated using a 1 M electrolyte solution of $LiPF_6$ in EC: DMC and lithium metal as a counter electrode. The cells were assembled in an Ar-filled glovebox (O_2 < 0.1 ppm, H_2O < 0.1 ppm) and tested in a battery cycler (BT-lab, Biologic) using the galvanostatic protocol. For galvanostatic intermitted titration technique (GITT) experiments, first, the cells were cycled at C/10 for three cycles then a current equivalent to a C/10 rate was applied for 1 h followed by a 4 h relaxation.

For *in-situ* XRD measurements, the $Nb_2(PO_4)_3$ anode was coated on pinhole-free thin aluminum foil (Alfa, 99.99%, 10 mm thickness) and a home-made *in-situ* cell fitted with Be-window was used for the experiment. XRD patterns at different state-of-charge were collected at the same Bruker D8-diffractometer and Le-Bail fitting was performed using the Fullprof program.

X-ray absorption spectroscopy (XAS) measurements of pristine and cycled electrodes at different state-of-charge were carried out at PETRA-III beamline P65 at DESY in Hamburg. The measurements of the Nb-K edge at room temperature were performed in fluorescence mode as well as transmission mode using gas ionization chambers to monitor the intensities of the incident and transmitted X-ray using a PIPS diode. The energy of the Nb-K edge was calibrated by defining the inflection point (first derivative maxima) of Nb foil as 18987.5 eV. Nb_2O_5 and NbO_2 were used as the standard materials. The standard materials were thoroughly mixed with boron nitride and pressed into 12 mm pellets of 1 mm thickness and the *ex-situ* electrodes were sealed in between Kapton tapes inside the Ar-filled glove box and used directly for the data collection. All data were

collected at room temperature with a Si (111) double crystal monochromator and all XAS spectra were processed using the DEMETER software package.[44,45]

Computations:

Density functional theory (DFT) calculations were performed using the Vienna ab initio simulation package (VASP),[46,47] which employs a plane wave basis (energy cut-off of 520 eV) and projector augmented wave[48] potentials. To describe the electronic exchange and correlation, we used the strongly constrained and appropriately normed[49] functional. We used a Γ-centred *k*-point mesh to sample the Brillouin zone with a density of at least 32 *k*-points per Å. We relaxed the lattice vectors, cell shape, and cell volume of all structures, without preserving the underlying symmetry, with structures considered converged when the total energies and atomic forces drop below 0.01 meV and |0.03| eV/Å. We obtained the initial structure of $Nb_2(PO_4)_3$ from the inorganic crystal structure database[50] and we took the equivalent Na positions from the $Na_4V_2(PO_4)_3$ cathode NASICON structure. The Na-vacancy orderings at $NaNb_2(PO_4)_3$, $Na_2Nb_2(PO_4)_3$, and $Na_3Nb_2(PO_4)_3$ compositions were enumerated using the pymatgen[51] package within the primitive cell (containing two $Nb_2(PO_4)_3$ formula units) and a $2 \times 1 \times 1$ supercell of the primitive NASICON structure. The procedure to calculate average voltages, which neglect pV and entropic contributions, is detailed in our previous works.[52,53]

Results and discussions

Polycrystalline NASICON-$Nb_2(PO_4)_3$ was prepared through the classical solid-state synthesis route using Nb_2O_5, Nb, and P_2O_5 precursors (for details, see Experimental section). Figure 1a shows the Rietveld refinement of the synchrotron X-ray diffraction (XRD) pattern collected on NASICON-$Nb_2(PO_4)_3$ at room temperature. The XRD pattern can be completely indexed with $R\bar{3}c$ space group, thus confirming the phase purity of the sample. Scanning electron microscopy (SEM) image of NASICON-$Nb_2(PO_4)_3$ (inset of Figure 1a) shows the presence of irregular micron-sized (~10 μm) primary particles and elemental mapping shows the homogenous distribution of Nb, P, and O in the sample (Figure S1). The calculated lattice parameters (a = 8.6629(1) and c = 22.0627(6) Å) and atomic coordinates of NASICON-$Nb_2(PO_4)_3$ structure are

displayed in Table S1 in the supplementary information.[42] Its crystal structure is built by lantern units, consisting of two (Nb^{5+}/Nb^{4+})O_6 and three PO_4 units, stacked along the *c*-direction (Figure 1b) and both Na(1) and Na(2) (i.e., 6b and 18e, respectively) sites are empty. To probe the oxidation state of Nb in the NASICON-$Nb_2(PO_4)_3$, X-ray absorption spectroscopy measurements were performed along with Nb_2O_5 and NbO_2 references. Their corresponding normalized X-ray near-edge spectra (XANES) collected at Nb K-edge are shown in Figure 1c. The absorption edge position of $Nb_2(PO_4)_3$ is found to be between those of Nb_2O_5 and NbO_2, thus confirming the presence of both Nb^{5+} and Nb^{4+} in the NASICON lattice.

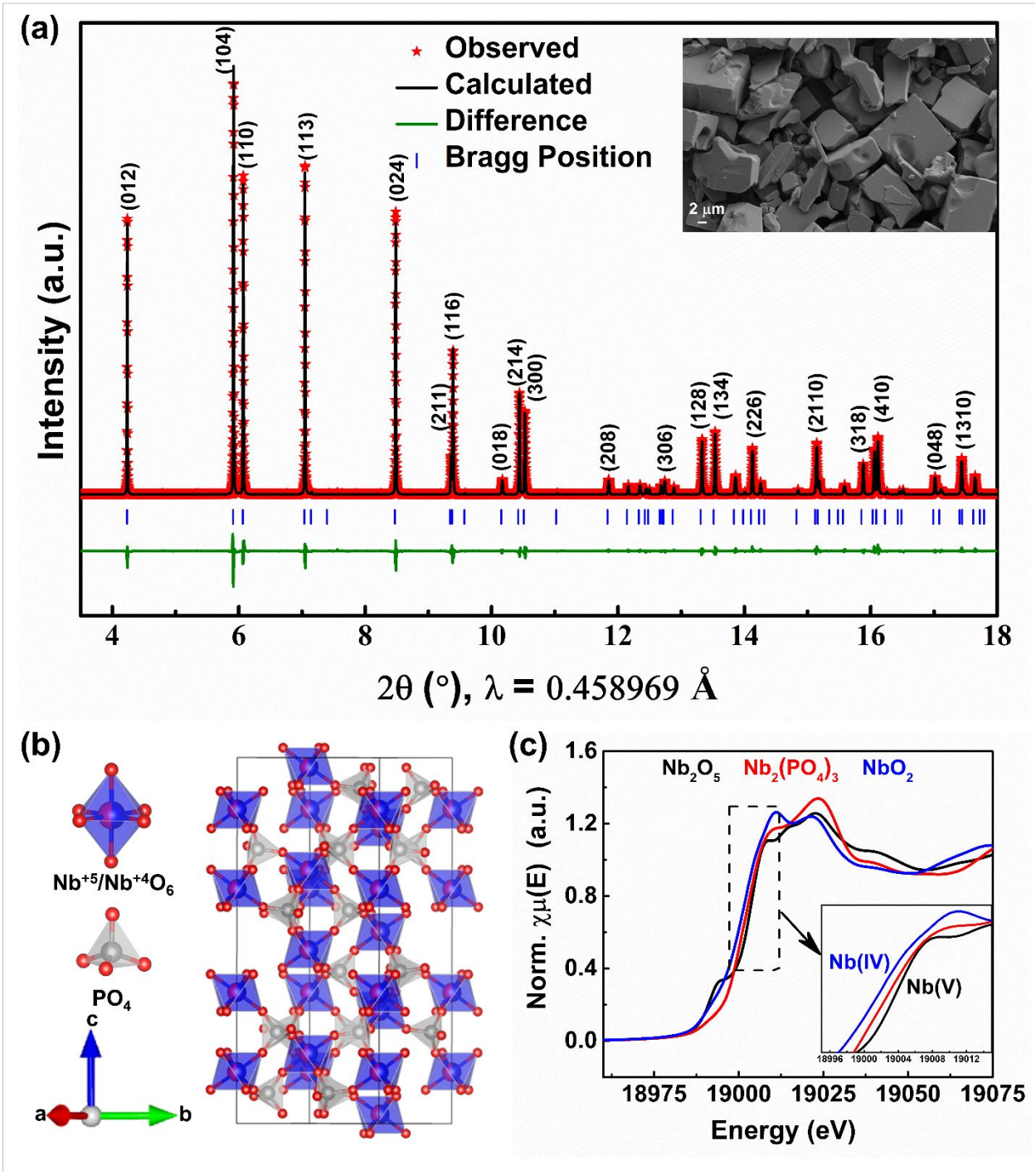

Figure 1. (a) Rietveld refinement of room temperature synchrotron XRD pattern (Inset: SEM image), (b) crystal structure, and (c) XANES collected at Nb K-edge of NASICON-$Nb_2(PO_4)_3$.

The NASICON-$Nb_2(PO_4)_3$ anode is expected to reversibly exchange three moles of Li- and Na-ions through redox activities Nb^{5+}/Nb^{4+} and Nb^{4+}/Nb^{3+} centers, leading to the theoretical

capacity of ~171 mAh g^{-1}. First, we studied the electrochemical Li-ion (de)intercalation property of NASICON-$Nb_2(PO_4)_3$ anode in Li half cells. The voltage-capacity plot of $Nb_2(PO_4)_3$/Li cell cycled at C/10 rate in the voltage window of 3.0-1.2 V vs. Li^+/Li^0 is displayed in Figure 2a. During the first discharge, this cell exhibits two voltage plateaus at ~2.3 and 1.6 V vs. Li^+/Li^0 followed by a slopping curve until 1.2 V vs. Li^+/Li^0 with a total discharge capacity of 257 mAh g^{-1}. On the subsequent charge, the two-step voltage profile is reversed with a charge capacity of 167 mAh g^{-1}, which is equivalent to the deintercalation of ~2.9 moles of Li-ions from the $Nb_2(PO_4)_3$ framework. Nearly 1.5 moles of lithium-ions are lost during the first cycle, which could be due to electrolyte decomposition. The voltage-capacity profiles from the subsequent cycles overlap with each other with capacities of ~167 mAh g^{-1}. The corresponding dQ/dV curves (Figure 2b) show two oxidation/reduction peaks located at 2.31/2.29 and 1.65/1.55 V vs. Li^+/Li^0, which could be tentatively assigned to the operation of Nb^{5+}/Nb^{4+} and Nb^{4+}/Nb^{3+} redox couples, respectively.

To better understand the structural evolution of NASICON-$Nb_2(PO_4)_3$ anode upon Li (de)intercalation, we performed an *in-situ* XRD measurement at C/15 rate during the first cycle (Figure 2c and d) and the evolution of corresponding lattice parameters is displayed in Figure 2e. Initially, a small solid-solution region is noticed for a $\Delta x = 0.2$ moles of Li-ion intercalation into NASICON-$Nb_2(PO_4)_3$ anode with subtle changes in the lattice parameters (Φ_A: $Li_{0\text{-}0.2}Nb_2(PO_4)_3$). As the discharge proceeds through the voltage plateau at ~2.25 V vs. Li^+/Li^0, we find a new set of reflections along with the parent NASICON-$Nb_2(PO_4)_3$, indicating a two-phase intercalation mechanism (Φ_B: $Li_{1.3\text{-}3.0}Nb_2(PO_4)_3$). However, the peak positions of both NASICON phases slightly drift as Li-ion intercalation proceeds, similar to $LiVOPO_4$ and $Na_3V_2(PO_4)_2F_3$ cathodes.[54,55] The XRD pattern collected at the end of 1.5 V shows anisotropic lattice parameter changes, i.e., $\Delta a/a = +1.21$ % and $\Delta c/c = -3.06$ %, with a nominal overall unit cell volume reduction of $\Delta v/v = -0.69$ %. Further, as the voltage descends to 1.2 V vs. Li^+/Li^0, we notice a smoother variation of peak positions, signifying solid-solution behavior. It is worth mentioning that the XRD patterns collected closer to 1.2 V present weaker reflections, implying the formation of short-range ordered "$Li_3Nb_2(PO_4)_3$" at the end of discharge. Note that the extra capacity (i.e., 4 moles of Li^+ insertion) observed during the first discharge can be accounted for electrolyte decomposition as mentioned earlier. The overall volume change between the fully lithiated and pristine NASICON phases is estimated as $\Delta v/v = +0.03$ %. Interestingly, upon subsequent charging the above-mentioned phenomena are reversed sequentially and the XRD pattern collected at the end of 1st

cycle nearly superimposes on that of the pristine electrode, indicating excellent reversibility of Li-ion (de)intercalation reaction. Further, the *in-situ* XRD patterns collected during the second cycle quite resemble the first cycle patterns, thus confirming the same Li-ion (de)intercalation pathway in the successive cycles (Figure S2). It is worth mentioning that the limited quality of XRD patterns impedes us to solve the crystal structures of Li-rich NASICON phases obtained during discharge, especially given the large configurational space for Li to arrange itself in the NASICON lattice. Thus, advanced local and bulk structural studies along with DFT calculations are required to elucidate the Li-ion (de)intercalation mechanism of the $Nb_2(PO_4)_3$ anode.

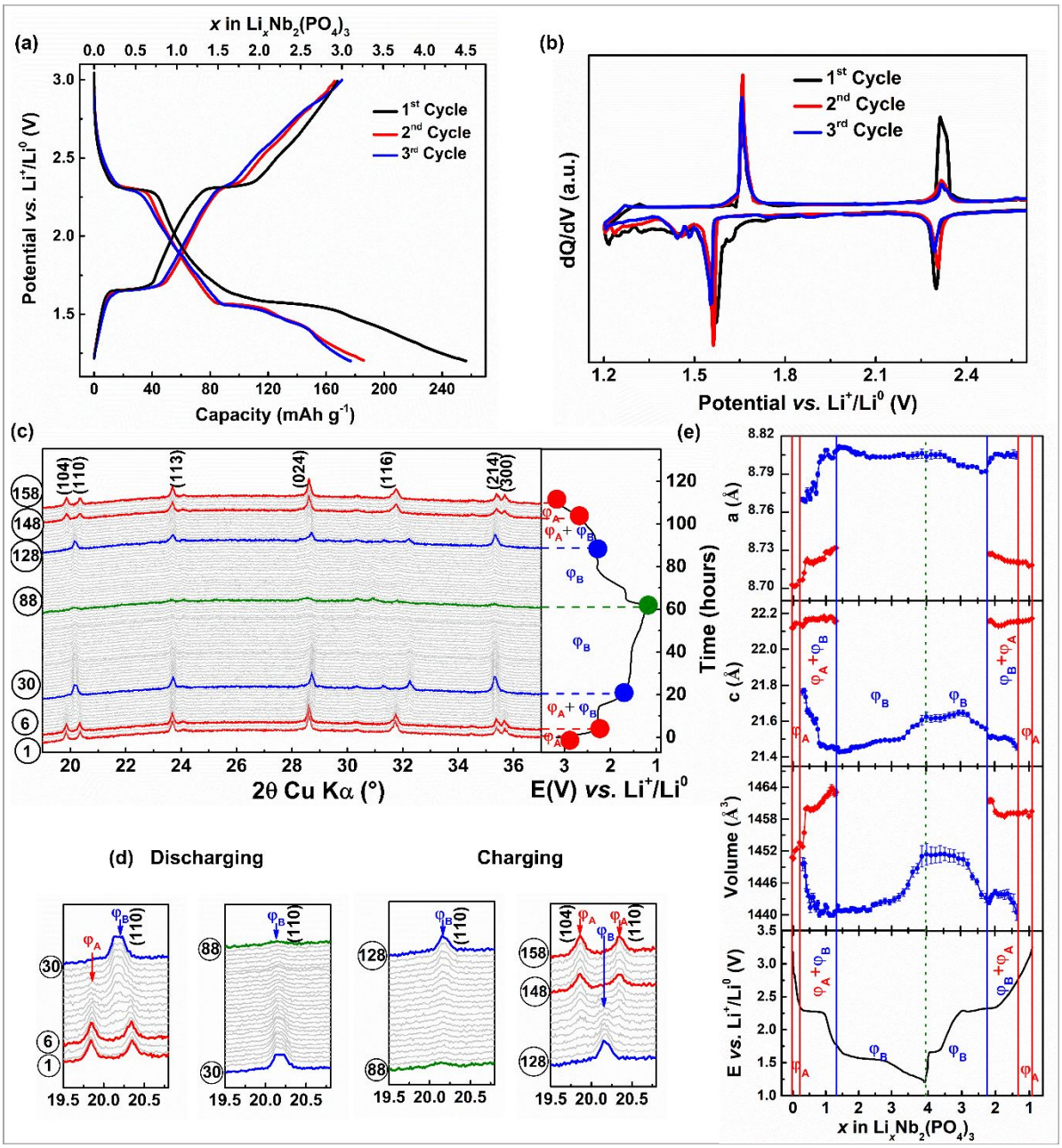

Figure 2. (a) Voltage vs. capacity and (b) dQ/dV profiles of $Nb_2(PO_4)_3$/Li cell. (c and d) *In-situ* XRD patterns of $Nb_2(PO_4)_3$ anode and (e) its cell parameter evolution during the first cycle of Li-ion (de)intercalation (vertical solid and dotted lines indicate the phase boundaries during Li-ion (de)intercalation).

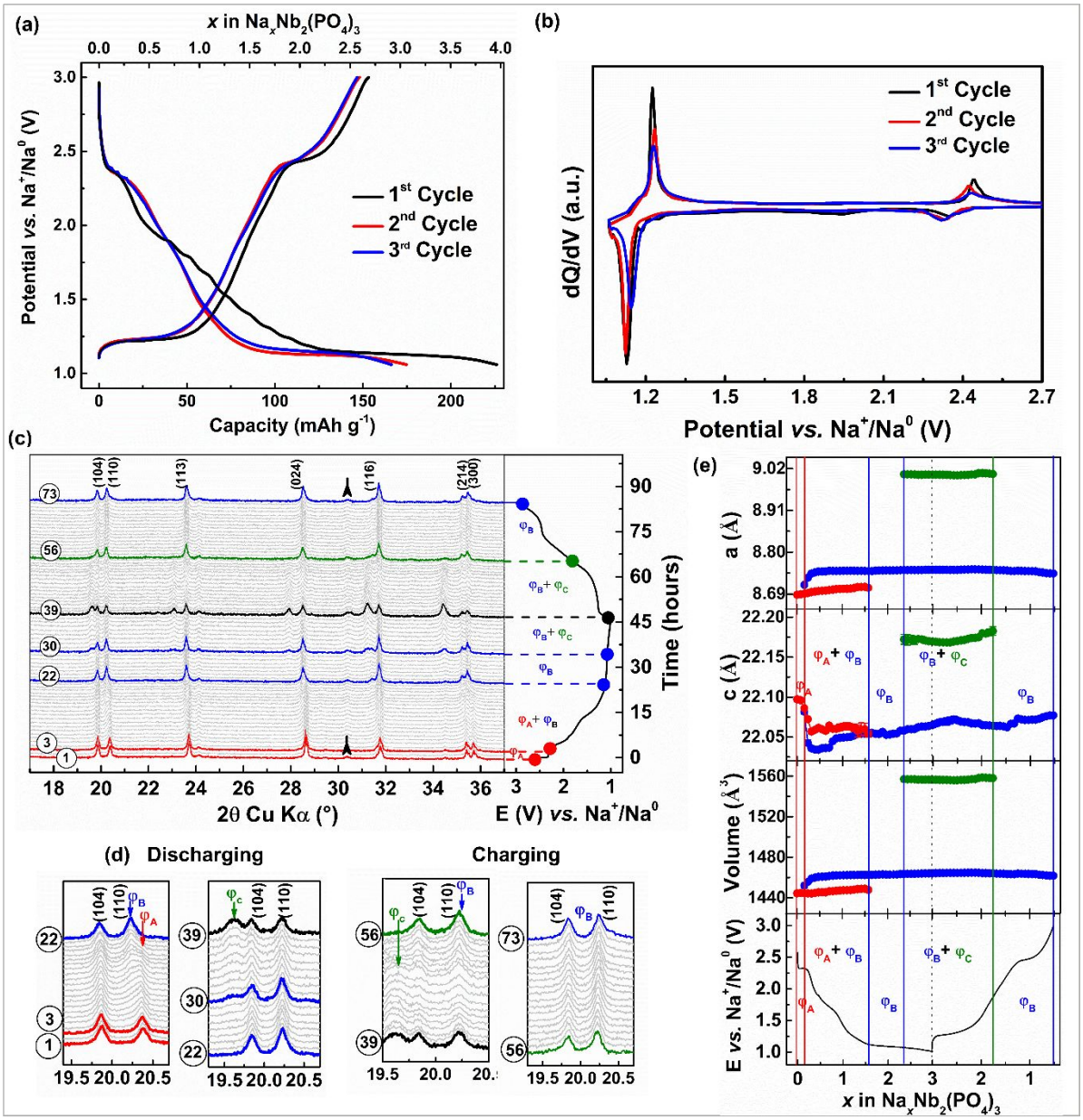

Figure 3. (a) Voltage vs. capacity and (b) dQ/dV profiles of $Nb_2(PO_4)_3$/Na cell. (c and d) *In-situ* XRD patterns of $Nb_2(PO_4)_3$ anode and (e) its cell parameter evolution during the first cycle of Na-ion (de)intercalation (vertical solid and dotted lines indicate the phase boundaries during Na-ion (de)intercalation).

The voltage-capacity profiles of $Nb_2(PO_4)_3$/Na cell cycled at C/10 rate in the window of 3.0-1.05 V vs. Na^+/Na^0 are displayed in Figure 3a. In contrast to its Li counterpart, the $Nb_2(PO_4)_3$/Na cell exhibits a shorter voltage step at ~2.35 V vs. Na^+/Na^0 (for $\Delta x = 0.2$ Na^+), which is followed by a slopping voltage curve until 1.2 V vs. Na^+/Na^0 (for $\Delta x = 2$ Na^+) and a voltage plateau at ~1.14 V vs. Na^+/Na^0 with a total discharge capacity of 226 mAh g^{-1}. During the

subsequent charge, these voltage features are partially reversible with a de-sodiation capacity of 150 mAh g^{-1} (i.e., equivalent to 2.6 moles of Na-ions deintercalation from $Nb_2(PO_4)_3$ framework). A capacity of 76 mAh g^{-1} is lost during the first cycle, which could be due to electrolyte decomposition and/or partial entrapment of Na^+ ions in the NASICON-$Nb_2(PO_4)_3$ framework.[56,57] The voltage-capacity profiles of the second and third cycles neatly superimpose on each other with reversible capacities and Coulombic efficiencies of ~150 mAh g^{-1} and 95 %, respectively. The corresponding dQ/dV profiles of the $Nb_2(PO_4)_3$/Na cell (Figure 3b) enlist two oxidation/reduction peaks located at 2.4/2.3 and 1.22/1.12 V vs. Na^+/Na^0 which could be attributed to the operation of Nb^{5+}/Nb^{4+} and Nb^{4+}/Nb^{3+} redox couples, respectively.

To follow the structural changes of the $Nb_2(PO_4)_3$ anode upon Na-ion (de)intercalation, we carried out an *in-situ* XRD measurement at the C/15 rate during the first cycle (Figure 3c and d). The calculated lattice parameters of the XRD patterns are plotted against x in Figure 3e. At the beginning of the first discharge (pattern #1-3), the formation of $Na_{0.2}Nb_2(PO_4)_3$ (denoted as Φ_A phase) from the parent $Nb_2(PO_4)_3$ proceeds *via* a solid-solution mechanism, which can be self-evident from moving of XRD peaks toward lower 2θ values. During this process, the changes in lattice parameters are less pronounced ($\Delta a/a$ = +0.03% and ($\Delta c/c$ = -0.05%). The decrease of the *c*-parameter can be attributed to the filling of Na-ions into the Na (1) site, which diminishes the electrostatic repulsion between NbO_6 octahedra. As the discharge proceeds to the next Δx = 1.4 (pattern #4-22), a new set of reflections belonging to another NASICON phase (Φ_B: $Na_{1.6-2.3}Nb_2(PO_4)_3$) grows at the expense of the former Φ_A phase (refer Figure 3e), which is followed by another narrow solid-solution region for Δx = 0.66 (Pattern #23-30). The *c*-parameters of both NASICON (Φ_A and Φ_B) phases initially decrease (due to the filling of Na (1) site) and stabilize whereas their *a*-parameters do not change significantly. Beyond this point, the sodiation reaction associated with the low-voltage plateau (1.15 V vs. Na^+/Na^0) continues *via* a two-phase mechanism, resulting in the formation of third NASICON phase "$Na_3Nb_2(PO_4)_3$" (denoted as Φ_C). During this process, the cell parameters and unit cell volume of Φ_C increase ($\Delta a/a$ = +3.64 %, %, $\Delta c/c$ = +0.32 %, and $\Delta v/v$ = +7.77 %) with the respect to the pristine NASICON phase. The increase of cell parameters can be correlated to the filling of sodium ions and the increase of NbO_6 octahedra size (due to the reduction of Nb^{5+}/ Nb^{4+} to Nb^{4+}/Nb^{3+}).

Further, we collected the synchrotron powder XRD pattern of the fully discharged $Na_3Nb_2(PO_4)_3$ (cycled at C/50 rate) to elucidate its crystal structure (Figures 4a and b). The XRD pattern can be completely indexed with ($P\bar{1}$) space group with the cell parameters: a = 8.7153(2) Å, b = 9.0908(1) Å, c = 22.6495(1)Å, α = 89.112(9)°, β = 90.052(9)° and γ = 119.912(3)°, similar to NASICON-$Na_3Ti_2(PO_4)_3$[58,59]. In this structure, sodium ions fully and partially occupy Na (1a-d) and Na(2a-f) sites which correspond to the Na (1) and Na(2) sites of the $R\bar{3}c$ structure, respectively. On the subsequent charge, the above-mentioned intercalation phenomena are mostly reversed, except the final XRD pattern (pattern #73) does not exactly match that of the pristine electrode. Indeed, its corresponding unit cell parameters and volume indicate the entrapment of Na-ions (~0.6 moles) in $Nb_2(PO_4)_3$, in agreement with our electrochemical results. Further, the *in-situ* XRD patterns collected during the second cycle display similar Na (de)intercalation phenomena as observed in the first cycle, confirming the reversibility of the (de)sodiation process (Figure S3).

To further understand the Na (de)intercalation phase behavior, we performed DFT calculations (see Methods section), with the calculated 0 K formation energy and voltage values plotted as a function of Na concentration (x) in $Nb_2(PO_4)_3$ in Figure 4c and d, respectively. The convex hull in Figure 4c indicates that the stable ground states of the $Na_xNb_2(PO_4)_3$ include the fully empty ($Nb_2(PO_4)_3$), fully sodiated ($Na_4Nb_2(PO_4)_3$), and partially sodiated ($Na_3Nb_2(PO_4)_3$) configurations. Importantly, the ground state at x = 3, is similar to the ground state configurations observed in other NASICON cathode chemistries.[52,53] The $Na_3Nb_2(PO_4)_3$ ground state has Na fully occupying the Na(1) site and partially occupying the Na(2) sites, which is in line with our experimental observation as well (Figure 4b). In contrast to other cathode chemistries, however, we don't observe a ground state configuration at x = 1,[52] which explains the minor solubility ($x \leq 0.2$) of Na in the empty $Nb_2(PO_4)_3$ structure. In terms of average voltages (Figure 4d), we predict a voltage plateau of ~1.06 V between x = 0 and 3, and ~0.93 V between x = 3 and 4, partly in agreement with our observed voltage plateau of ~1.15 V vs. Na that represents a two-phase intercalation mechanism as well. Experimentally, we observe capacity degradation to occur whenever we attempt to cycle the $Na_xNb_2(PO_4)_3$ system below 1 V vs. Na. This capacity degradation can be due to electrolyte degradation and/or Na-entrapment. Note that computationally, we have calculated a two-phase voltage plateau to form at voltages below 1 V vs. Na, which will result in the formation of the $Na_4Nb_2(PO_4)_3$ phase. Previous computational studies on NASICON systems[60] showed that

the Na conductivity (or diffusivity) drops significantly as Na content in NASICONs approach x_{Na} = 4. Moreover, the redox behavior may not be fully reversible from Nb^{2+} till Nb^{4+}, as reported with other transition metals as well within the NASICON framework[53]. Hence, we expect partial entrapment of Na to occur at voltage ranges below 1 V vs. Na, due to the formation of the $Na_4Nb_2(PO_4)_3$ phase.

To monitor the changes in the Nb oxidation state and local structure, we performed X-ray absorption spectroscopy measurements. Figure 4e displays the normalized XANES spectra of pristine, discharged, and charged electrodes collected at Nb K-edge. As the discharge proceeds the XANES of Nb K-edge shifts towards lower energy values, indicating the reduction of Nb^{5+}/Nb^{4+} to Nb^{4+}/Nb^{3+}, and subsequently moves back to higher energy values at the end of the first charge. The corresponding Fourier-transformed extended X-ray absorption fine structure (EXAFS) plots are displayed in Figure 4f. The peak located at 1.5 Å corresponds to the Nb-O shell, whereas the next three peaks located in between ~2.0-3.25 Å represent the second and third shells of Nb-P and Nb-Na pairs. The EXAFS collected at the end of discharge shift towards higher Å values, indicating the expansion of the NASICON structure. Note that although the EXAFS collected on the subsequent discharge shifts towards lower Å values, it doesn't coincide with that of the pristine electrode due to the entrapment of Na-ions in the NASICON framework. These observations are in agreement with our electrochemical and *in-situ* XRD results. Further, the fitting of EXAFS oscillations shows the increase of average Nb-O bond length from 2.028 to 2.086 Å during discharge due to the reduction of niobium.

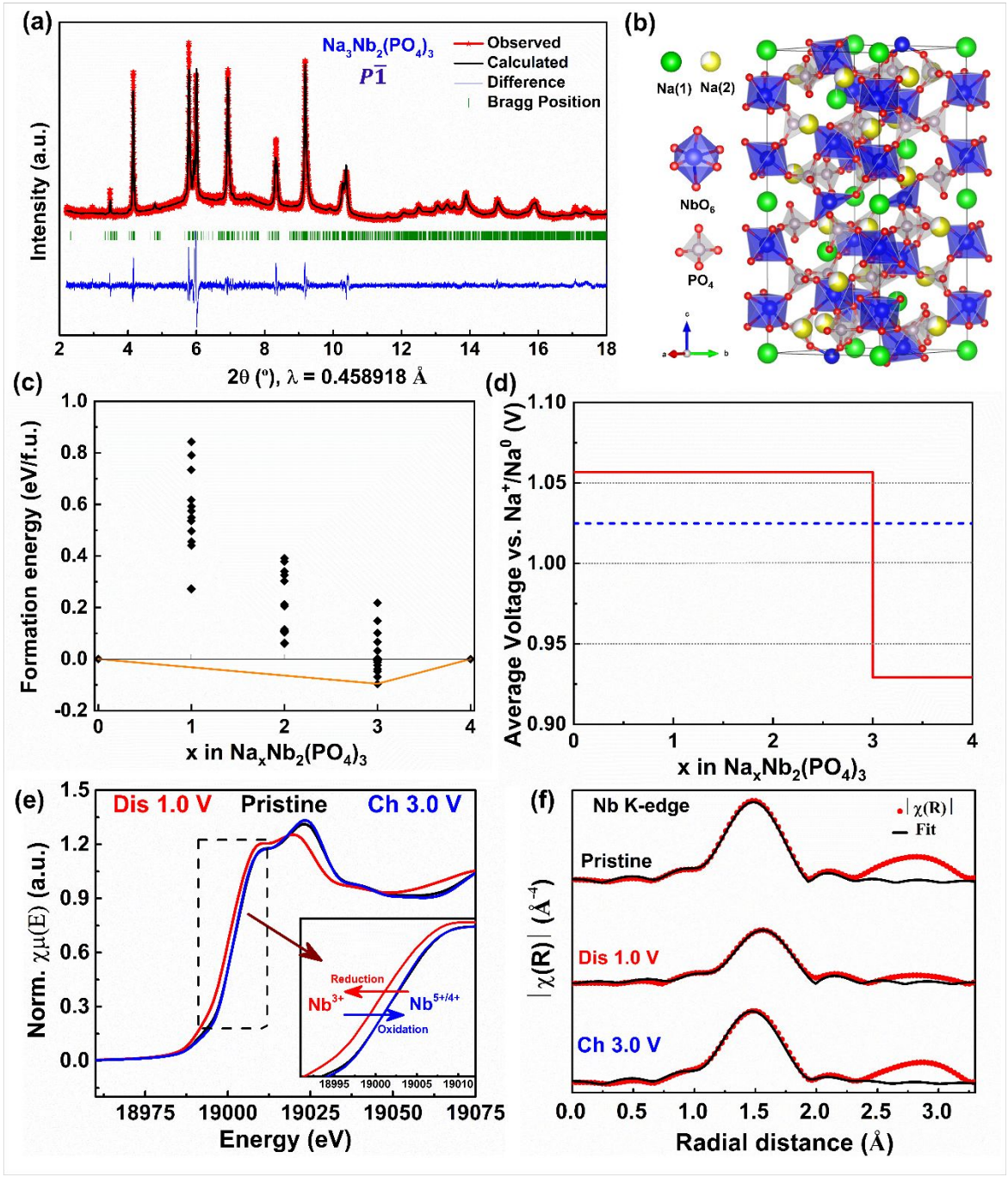

Figure 4. (a) Le Bail refinement of synchrotron XRD and (b) crystal structure of $Na_3Nb_2(PO_4)_3$. (c) 0 K formation energy and (d) voltage plots (vs. Na) as a function of Na concentration (x) in $Na_xNb_2(PO_4)_3$ formula unit. The formation energy in (c) is referenced to the $Nb_2(PO_4)_3$ (fully empty) and $Na_4Nb_2(PO_4)_3$ (fully sodiated) compositions. The orange line in (c) indicates the convex hull, i.e., the collection of lowest energy Na-vacancy configurations in $Na_xNb_2(PO_4)_3$, while the black diamonds indicate metastable configurations. The dashed black line in (d) overall

average voltage across the entire Na concentration in $Nb_2(PO_4)_3$ (e) XANES and (f) EXAFS plots of NASICON-$Nb_2(PO_4)_3$ anode collected at Nb K-edge.

Our combined electrochemical and *in-situ* experiments highlight the distinct intercalation behavior of the same NASICON-$Nb_2(PO_4)_3$ anode against Li and Na. For instance, the $Nb_2(PO_4)_3$/Li and $Nb_2(PO_4)_3$/Na cells exhibit flat and slopping voltage curves for the initial one mole of Li and Na ion intercalation, respectively, even though both mostly follow a two-phase mechanism. Moreover, the volume of the $Nb_2(PO_4)_3$ unit cell shrinks along with the loss of long-range crystal order during the low voltage lithiation (~at 1.55 V vs. Li^+/Li^0) whereas the same anode exhibits volume expansion upon the low voltage sodiation (at ~1.1 V vs. Na^+/Na^0). Hence, to better comprehend the Li and Na intercalation mechanism of NASICON-$Nb_2(PO_4)_3$ anode, we performed galvanostatic intermittent titration technique (GITT) experiments during the fourth cycle (see Experimental for details, Figure 5a and b).

Notably, both Li and Na GITT voltage vs. composition (x in $Li_xNb_2(PO_4)_3$ or $Na_xNb_2(PO_4)_3$) profiles present significant polarization between charge and discharge processes (even after 4 h relaxation). More importantly, the voltage jumps during the open circuit voltage (OCV) steps are prominent during charging compared to discharging process, which is also reflected by the steep increase of internal resistance values and can be ascribed to slower solid-state Li and Na ion diffusion.[61,62] Such a difference could arise from various thermodynamic and kinetic factors involving structural and electrochemical properties of the NASICON host. As mentioned earlier, Li and Na ions prefer to occupy different crystallographic sites, which have distinct (electro)chemical potentials for (de)intercalation.[63] Moreover, it is well known that ionic conduction in the NASICON framework occurs *via* correlated ion migration through M(1)/M(2) pathways,[24,64] thus the relative filling of these sites can tune ionic conductivities and intercalation kinetics. Besides, the different chemical characters of Li and Na ions (i.e., relative polarizability) can impart a different degree of interactions with the host lattice (such as distortion of polyhedral units),[65] which can lead to stabilization of various intermediates including lower symmetry structures (C2/c and $P\bar{1}$ as in the cases of $Na_3V_2(PO_4)_3$ and $Na_3Nb_2(PO_4)_3$, respectively)[59,63,66] during cycling, leading to distinct electrochemical Li and Na intercalation pathways. Nevertheless, comprehensive studies involving short-range and long-range structural probes and DFT

calculations are required to fully elucidate the structure-property relationship of the $Nb_2(PO_4)_3$ anode.

Lastly, we have evaluated the rate performances and cycling stabilities of $Nb_2(PO_4)_3$/Li and $Nb_2(PO_4)_3$/Na cells at different C-rates. The $Nb_2(PO_4)_3$/Li cell delivers discharge capacities of 186, 174, 164, 155, and 142 mAh g-1 at C/10, C/5, C/2, 1C, and 2C rates, respectively, whereas the $Nb_2(PO_4)_3$/Na cell shows capacities of 172, 163, 153, 144 and 129 mAh g^{-1} under similar experimental conditions (Figure 5c). Upon cycling at the C/10 rate, the $Nb_2(PO_4)_3$/Li and $Nb_2(PO_4)_3$/Na cells exhibit stable discharge capacities greater than 184 and 156 mAh g^{-1}, respectively, for 20 cycles (Figure 5d). Further, we assessed their cycling stability at 1 C rate (Figure 5e). The $Nb_2(PO_4)_3$/Li and $Nb_2(PO_4)_3$/Na cells exhibit first/second cycle discharge capacities of 227/161 and 179/142 mAh g^{-1}, respectively. The large discrepancies in discharge capacities between the first and second cycles can be attributed to the electrolyte decomposition and the entrapment of Li and Na ions in the NASICON framework. In the subsequent cycles, the discharge capacities of $Nb_2(PO_4)_3$/Li cell slowly decrease and stabilize around 122 mAh g^{-1} (after 100 cycles) and the cell still delivers a discharge capacity of 100 mAh g^{-1} after 200 cycles. The $Nb_2(PO_4)_3$/Na cell retains 60.2% of its second discharge capacity after 200 cycles. The lower capacities obtained at high C-rate could be due to micron-size active particles in the as-prepared anode (Figure S4). It is also worth mentioning here that upon lowering the discharge voltage to 0.9 V, the capacity decay is faster in $Nb_2(PO_4)_3$/Na cells due to significant electrolyte degradation (Figure S5). Further studies to improve the cycling performance of $Nb_2(PO_4)_3$ anode as well as to build full Li- and Na-ion cells are in progress. It is important to note that the integration of NASICON-$Nb_2(PO_4)_3$ anode and NASICON-$Na_3V_2(PO_4)_3$ cathode with a suitable electrolyte is expected to produce a higher energy density Na-ion battery compared to the Ti- and V-based anodes (Figure S6).[67]

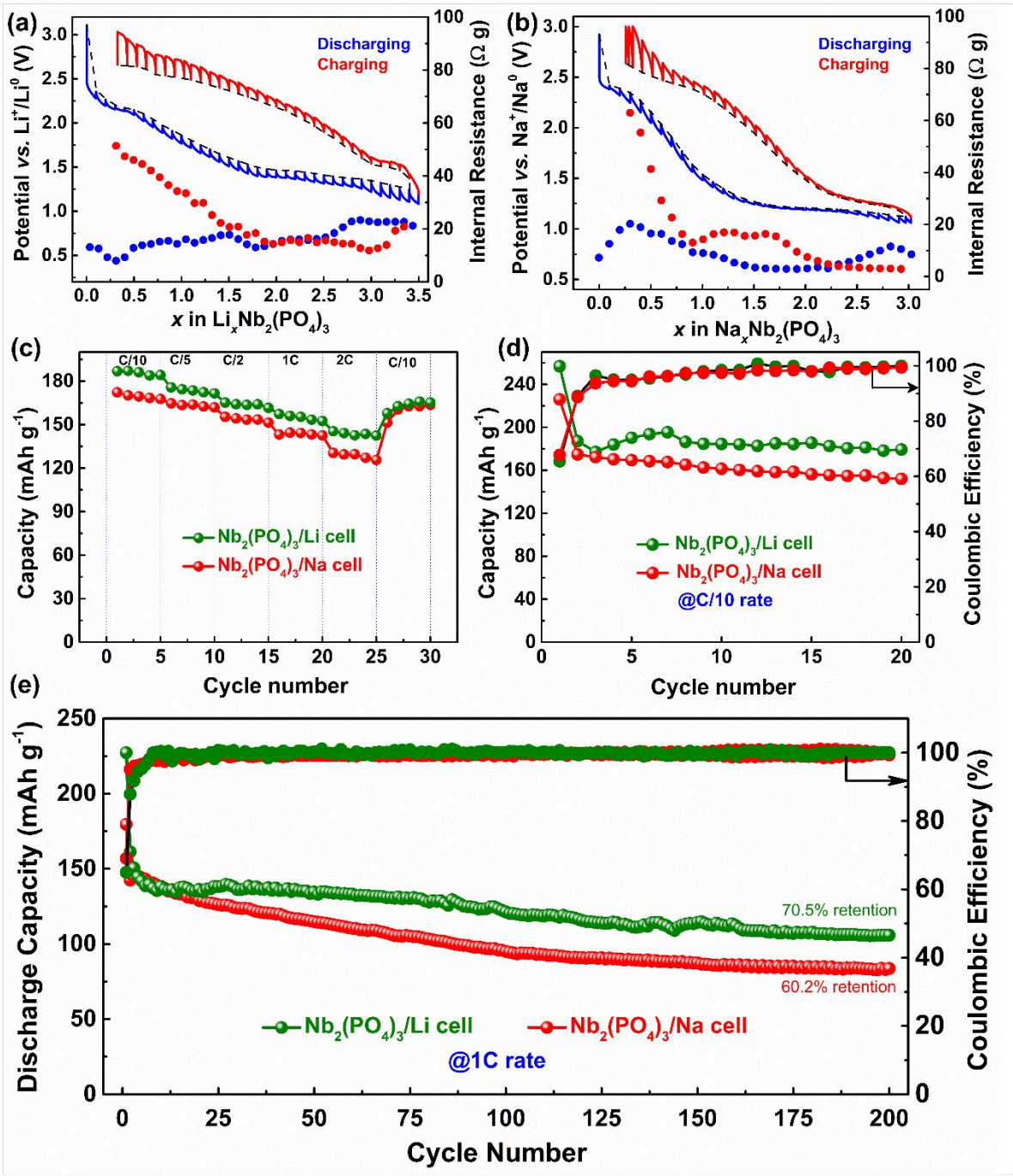

Figure 5. GITT curve and calculated internal resistance for (a) $Nb_2(PO_4)_3$/Li and (b) $Nb_2(PO_4)_3$/Na cells. Rate capability (c), capacity retention at C/10 (d) and 1 C (e) plots of $Nb_2(PO_4)_3$/Li and $Nb_2(PO_4)_3$/Na cells.

Conclusion

In conclusion, we have successfully synthesized polycrystalline $Nb_2(PO_4)_3$ and demonstrated its potential application as an anode material for Li- and Na-ion batteries. The NASICON-$Nb_2(PO_4)_3$ reversibly exchanged Li and Na ions at average voltages of 1.86 V and 1.46 V vs. Li^+/Li^0 and Na^+/Na^0 with intercalation capacities of ~167 and 150 mAh g^{-1}, respectively. Our *in-situ* XRD measurements revealed multiple-phase transformations during Li and Na intercalation with the formation of short-range ordered $Li_3Nb_2(PO_4)_3$ and triclinic ($P\bar{1}$)-$Na_3Nb_2(PO_4)_3$ at the end of discharge. Our DFT calculations predicted the $Na_3Nb_2(PO_4)_3$ composition to be stable in the Na-$Nb_2(PO_4)_3$ pseudo-binary system, in agreement with the *in-situ* XRD measurements. The distinct electrochemical Li and Na intercalation behavior of the $Nb_2(PO_4)_3$ anode can be ascribed to the relative differences in size, filling of crystallographic sites and chemical characters of Li and Na ions. Although the micron-sized anode showed moderate storage capacities (~106 and 84 mAh g^{-1} for Li and Na cells, respectively) at higher C-rate (1 C) after 200 cycles, further optimization of electrode and electrolytes is expected to produce better performance, which can aid in building high energy density Na-ion battery.

Supporting Information

Supporting Information is available from the RSC webpage.

Acknowledgments

This work was supported by the Department of Science & Technology (DST), Government of India (DST/TMD/MES/2K18/188). The authors acknowledge DESY (Hamburg, Germany), a member of the Helmholtz Association HGF, for the provision of experimental facilities. Parts of this research were carried out at PETRA III and the authors thank Dr. Edmund Welter for his assistance in using Beamline P65 to perform X-ray absorption spectroscopy measurements and DST for financial assistance for the measurement at DESY. Synchrotron X-ray diffraction data were collected at 11-BM (mail-in program; GUP-77942), at the Advanced Photon Source, Argonne National Laboratory, a U.S. Department of Energy (DOE) Office of Science User Facility operated for the DOE Office of Science by Argonne National Laboratory under Contract No. DE-AC02-06CH11357.

Conflict of Interest

The authors declare no conflict of interest.

Author Contributions
All authors have approved the final version of the manuscript.

Keywords

Lithium- and sodium-ion batteries, NASICON, $Nb_2(PO_4)_3$, and multi-redox anode.

Author Information

Corresponding Author
*E-mail: prem@jncasr.ac.in

ORCID

Premkumar Senguttuvan: 0000-0001-8465-5896
Biplab Patra: 0000-0001-6340-0747
Gopalakrishnan Sai Gautam: 0000-0002-1303-0976

References

1 Z. Yang, J. Zhang, M. C. W. Kintner-Meyer, X. Lu, D. Choi, J. P. Lemmon and J. Liu, *Chem. Rev.*, 2011, **111**, 3577–3613.

2 B. Dunn, H. Kamath and J. M. Tarascon, *Science*, 2011, **334**, 928–935.

3 T. Kim, W. Song, D. Y. Son, L. K. Ono and Y. Qi, *J. Mater. Chem. A*, 2019, **7**, 2942–2964.

4 Y. Tian, G. Zeng, A. Rutt, T. Shi, H. Kim, J. Wang, J. Koettgen, Y. Sun, B. Ouyang, T. Chen, Z. Lun, Z. Rong, K. Persson and G. Ceder, *Chem. Rev.*, 2021, **121**, 1623–1669.

5 N. Tapia-Ruiz, A. R. Armstrong, H. Alptekin, M. A. Amores, H. Au, J. Barker, R. Boston, W. R. Brant, J. M. Brittain, Y. Chen, M. Chhowalla, Y. S. Choi, S. I. R. Costa, M. C.

Ribadeneyra, S. A. Cussen, E. J. Cussen, W. I. F. David, A. V. Desai, S. A. M. Dickson, E. I. Eweka, J. D. Forero-Saboya, C. P. Grey, J. M. Griffin, P. Gross, X. Hua, J. T. S. Irvine, P. Johansson, M. O. Jones, M. Karlsmo, E. Kendrick, E. Kim, O. V. Kolosov, Z. Li, S. F. L. Mertens, R. Mogensen, L. Monconduit, R. E. Morris, A. J. Naylor, S. Nikman, C. A. O'Keefe, D. M. C. Ould, R. G. Palgrave, P. Poizot, A. Ponrouch, S. Renault, E. M. Reynolds, A. Rudola, R. Sayers, D. O. Scanlon, S. Sen, V. R. Seymour, B. Silván, M. T. Sougrati, L. Stievano, G. S. Stone, C. I. Thomas, M. M. Titirici, J. Tong, T. J. Wood, D. S. Wright and R. Younesi, *J. Phys. Energy*, 2021, **3**, 031503.

6 K. Chayambuka, G. Mulder, D. L. Danilov and P. H. L. Notten, *Adv. Energy Mater.*, 2020, **10**, 2001310.

7 E. Goikolea, V. Palomares, S. Wang, I. R. de Larramendi, X. Guo, G. Wang and T. Rojo, *Adv. Energy Mater.*, 2020, **10**, 2002055.

8 J. M. Tarascon, *Joule*, 2020, **4**, 1616–1620.

9 E. Irisarri, A. Ponrouch and M. R. Palacin, *J. Electrochem. Soc.*, 2015, **162**, A2476–A2482.

10 G. N. Zhu, Y. G. Wang and Y. Y. Xia, *Energy Environ. Sci.*, 2012, **5**, 6652–6667.

11 K. M. Colbow, J. R. Dahn and R. R. Haering, *J. Power Sources*, 1989, **26**, 397–402.

12 J. F. Colin, V. Pralong, M. Hervieu, V. Caignaert and B. Raveau, *Chem. Mater.*, 2008, **20**, 1534–1540.

13 B. Guo, X. Yu, X. G. Sun, M. Chi, Z. A. Qiao, J. Liu, Y. S. Hu, X. Q. Yang, J. B. Goodenough and S. Dai, *Energy Environ. Sci.*, 2014, **7**, 2220–2226.

14 S. Qian, H. Yu, L. Yan, H. Zhu, X. Cheng, Y. Xie, N. Long, M. Shui and J. Shu, *ACS Appl. Mater. Interfaces*, 2017, **9**, 30608–30616.

15 Q. Cheng, J. Liang, Y. Zhu, L. Si, C. Guo and Y. Qian, *J. Mater. Chem. A*, 2014, **2**, 17258–17262.

16 P. Senguttuvan, G. Rousse, V. Seznec, J. M. Tarascon and M. R. Palacín, *Chem. Mater.*, 2011, **23**, 4109–4111.

17 W. Wang, Y. Liu, X. Wu, J. Wang, L. Fu, Y. Zhu, Y. Wu and X. Liu, *Adv. Mater. Technol.*, 2018, **3**, 1800004.

18 Y. Sun, L. Zhao, H. Pan, X. Lu, L. Gu, Y. S. Hu, H. Li, M. Armand, Y. Ikuhara, L. Chen and X. Huang, *Nat. Commun.*, 2013, **4**, 1870.

19 H. Gao and J. B. Goodenough, *Angew. Chemie Int. Ed.*, 2016, **55**, 12768–12772.

20 J. Wang, Y. Wang, D. H. Seo, T. Shi, S. Chen, Y. Tian, H. Kim and G. Ceder, *Adv. Energy Mater.*, 2020, **10**, 1–10.

21 S. Ghosh, N. Barman, M. Mazumder, S. K. Pati, G. Rousse and P. Senguttuvan, *Adv. Energy Mater.*, 2020, **10**, 1902918.

22 S. Chen, C. Wu, L. Shen, C. Zhu, Y. Huang, K. Xi, J. Maier and Y. Yu, *Adv. Mater.*, 2017, **29**, 1700431.

23 Z. Jian, Y. S. Hu, X. Ji and W. Chen, *Adv. Mater.*, 2017, **29**, 1601925.

24 M. Guin and F. Tietz, *J. Power Sources*, 2015, **273**, 1056–1064.

25 Z. Zhang, Z. Zou, K. Kaup, R. Xiao, S. Shi, M. Avdeev, Y. S. Hu, D. Wang, B. He, H. Li, X. Huang, L. F. Nazar and L. Chen, *Adv. Energy Mater.*, 2019, **9**, 1–14.

26 Z. Deng, G. Sai Gautam, S. K. Kolli, J. N. Chotard, A. K. Cheetham, C. Masquelier and P. Canepa, *Chem. Mater.*, 2020, **32**, 7908–7920.

27 R. Kahlaoui, K. Arbi, I. Sobrados, R. Jimenez, J. Sanz and R. Ternane, *Inorg. Chem.*, 2017, **56**, 1216–1224.

28 C. Masquelier, C. Wurm, J. Rodríguez-Carvajal, J. Gaubicher and L. Nazar, *Chem. Mater.*, 2000, **12**, 525–532.

29 A. Aatiq, M. Ménétrier, L. Croguennec, E. Suard and C. Delmas, *J. Mater. Chem.*, 2002, **12**, 2971–2978.

30 C. Delmas, F. Cherkaoui, A. Nadiri and P. Hagenmuller, *Mater. Res. Bull.*, 1987, **22**, 631–639.

31 S. Patoux and C. Masquelier, *Chem. Mater.*, 2002, **14**, 5057–5068.

32 M. Wu, W. Ni, J. Hu and J. Ma, *Nano-Micro Lett.*, 2019, **11**, 1–36.

33 P. Senguttuvan, G. Rousse, M. E. Arroyo Y De Dompablo, H. Vezin, J. M. Tarascon and M. R. Palacín, *J. Am. Chem. Soc.*, 2013, **135**, 3897–3903.

34 Z. Jian, L. Zhao, H. Pan, Y. S. Hu, H. Li, W. Chen and L. Chen, *Electrochem. commun.*, 2012, **14**, 86–89.

35 Z. Jian, W. Han, X. Lu, H. Yang, Y.-S. Hu, J. Zhou, Z. Zhou, J. Li, W. Chen, D. Chen, L. Chen, Z. L. Jian, W. Z. Han, X. Lu, H. X. Yang, Y. Hu, J. Q. Li, L. Q. Chen, J. Zhou, W. Chen, D. F. Chen and Z. B. Zhou, *Adv. Energy Mater.*, 2013, **3**, 156–160.

36 O. Tillement, J. C. Couturier, J. Angenault and M. Quarton, *Solid State Ionics*, 1991, **48**, 249–255.

37 J. Liu, K. Lin, Y. Zhao, Y. Zhou, X. Hou, X. Liu, H. Lou, K. H. Lam and F. Chen, *J. Mater. Chem. A*, 2021, **9**, 10437–10446.

38 S. Ghosh, N. Jose, B. Senthilkumar, P. Amonpattaratkit and P. Senguttuvan, *J. Electrochem. Soc.*, 2021, **168**, 050534.

39 T. Zhu, P. Hu, X. Wang, Z. Liu, W. Luo, K. A. Owusu, W. Cao, C. Shi, J. Li, L. Zhou and L. Mai, *Adv. Energy Mater.*, 2019, **9**, 2–7.

40 I. V. Zatovsky, *Acta Crystallogr. Sect. E*, 2010, **66**, i12.

41 B. Ouyang, J. Wang, T. He, C. J. Bartel, H. Huo, Y. Wang, V. Lacivita, H. Kim and G. Ceder, *Nat. Commun.*, 2021, **12**, 1–11.

42 A. Leclaire, M.-M. Borel, A. Grandin and B. Raveau, *Acta Crystallogr. Sect. C*, 1989, **45**, 699–701.

43 J. Rodríguez-Carvajal, *Phys. B Condens. Matter*, 1993, **192**, 55–69.

44 M. Newville, *J. Synchrotron Radiat.*, 2001, **8**, 322–324.

45 B. Ravel and M. Newville, *J. Synchrotron Radiat.*, 2005, **12**, 537–541.

46 G. Kresse and J. Hafner, *Phys. Rev. B*, 1993, **47**, 558.

47 G. Kresse and J. Furthmüller, *Phys. Rev. B*, 1996, **54**, 11169.

48 G. Kresse and D. Joubert, *Phys. Rev. B*, 1999, **59**, 1758.

49 J. Sun, A. Ruzsinszky and J. Perdew, *Phys. Rev. Lett.*, 2015, **115**, 036402.

50 M. Hellenbrandt, *Crystallogr. Rev.*, 2004, **10**, 17–22.

51 S. P. Ong, W. D. Richards, A. Jain, G. Hautier, M. Kocher, S. Cholia, D. Gunter, V. L. Chevrier, K. A. Persson and G. Ceder, *Comput. Mater. Sci.*, 2013, **68**, 314–319.

52 B. Singh, Z. Wang, S. Park, G. S. Gautam, J. N. Chotard, L. Croguennec, D. Carlier, A. K. Cheetham, C. Masquelier and P. Canepa, *J. Mater. Chem. A*, 2021, **9**, 281–292.

53 Z. Wang, S. Park, Z. Deng, D. Carlier, J. N. Chotard, L. Croguennec, G. S. Gautam, A. K. Cheetham, C. Masquelier and P. Canepa, *J. Mater. Chem. A*, 2022, **10**, 209–217.

54 M. Bianchini, F. Fauth, N. Brisset, F. Weill, E. Suard, C. Masquelier and L. Croguennec, *Chem. Mater.*, 2015, **27**, 3009–3020.

55 M. Bianchini, J. M. Ateba-Mba, P. Dagault, E. Bogdan, D. Carlier, E. Suard, C. Masquelier and L. Croguennec, *J. Mater. Chem. A*, 2014, **2**, 10182–10192.

56 M. Galceran, J. Rikarte, M. Zarrabeitia, M. C. Pujol, M. Aguiló and M. Casas-Cabanas, *ACS Appl. Energy Mater.*, 2019, **2**, 1923–1931.

57 P. Senguttuvan, G. Rousse, H. Vezin, J. M. Tarascon and M. R. Palacín, *Chem. Mater.*, 2013, **25**, 2391–2393.

58 H. Kabbour, D. Coillot, M. Colmont, C. Masquelier and O. Mentré, *J. Am. Chem. Soc.*, 2011, **133**, 11900–11903.

59 P. Senguttuvan, G. Rousse, M. E. Arroyo Y De Dompablo, H. Vezin, J. M. Tarascon and M. R. Palacín, *J. Am. Chem. Soc.*, 2013, **135**, 3897–3903.

60 Z. Deng, T. P. Mishra, E. Mahayoni, Q. Ma, A. J. K. Tieu, O. Guillon, J. N. Chotard, V. Seznec, A. K. Cheetham, C. Masquelier, G. S. Gautam and P. Canepa, *Nat. Commun.*, 2022, **13**, 1–14.

61 G. Yan, S. Mariyappan, G. Rousse, Q. Jacquet, M. Deschamps, R. David, B. Mirvaux, J. W. Freeland and J. M. Tarascon, *Nat. Commun.*, 2019, **10**, 585.

62 J. Kim, W. Lee, J. Seok, E. Lee, W. Choi, H. Park, S. Yun, M. Kim, J. Lim and W. S. Yoon, *J. Energy Chem.*, 2022, **66**, 226–236.

63 C. Masquelier, C. Wurm, J. Rodríguez-Carvajal, J. Gaubicher and L. Nazar, *Chem. Mater.*, 2000, **12**, 525–532.

64 Z. Zhang, Z. Zou, K. Kaup, R. Xiao, S. Shi, M. Avdeev, Y. S. Hu, D. Wang, B. He, H. Li, X. Huang, L. F. Nazar and L. Chen, *Adv. Energy Mater.*, 2019, **9**, 1902373.

65 S. Zhou, G. Barim, B. J. Morgan, B. C. Melot and R. L. Brutchey, *Chem. Mater.*, 2016, **28**, 4492–4500.

66 J. N. Chotard, G. Rousse, R. David, O. Mentré, M. Courty and C. Masquelier, *Chem. Mater.*, 2015, **27**, 5982–5987.

67 M. K. Sadan, A. K. Haridas, H. Kim, C. Kim, G. B. Cho, K. K. Cho, J. H. Ahn and H. J. Ahn, *Nanoscale Adv.*, 2020, **2**, 5166–5170.